Fast, Robust, and Faithful Methods for Detecting Crest Lines on Meshes

Shin Yoshizawa [a,*], Alexander Belyaev [b], Hideo Yokota [a], Hans-Peter Seidel [c]

[a]*RIKEN, 2-1, Hirosawa, Wako, Saitama, 351-0198, Japan*

[b]*Heriot-Watt University, Edinburgh, EH14 4AS, United Kingdom*

[c]*MPI Informatik, Stuhlsatzenhausweg 85, 66123 Saarbrücken, Germany*

Abstract

The crest lines, salient subsets of the extrema of the principal curvatures over their corresponding curvature lines, are powerful shape descriptors which are widely used for shape matching, interrogation, and visualization purposes. In this paper, we develop fast, accurate, and reliable methods for detecting the crest lines on surfaces approximated by dense triangle meshes. The methods exploit intrinsic geometric properties of the curvature extrema and provide with an inherent level-of-detail control of the detected crest lines. As an immediate application, we use of the crest lines for adaptive mesh simplification purposes.

Key words: ridges, crest lines, focal surfaces, Möbius-invariant energies, surface Laplacian

1 Introduction

Previous work. Surface creases, curves on a surface along which the surface bends sharply can be intuitively defined as loci of sharp variation points of the surface normal. Mathematically the sharp variation points of the surface normals are described via extrema of the surface principal curvatures along their corresponding lines of curvature. The full set of such extrema, frequently called *ridges* (Porteous, 1987), corresponds to the edges of regression of the envelopes of the surface normals and was first studied by A. Gullstrand in connection with his work in ophthalmology (1911 Nobel Prize in Physiology and Medicine). Since then the ridges

* Corresponding author: Dr. Shin Yoshizawa, Bio-research Infrastructure Construction Team, VCAD System Research Program, RIKEN, 2-1, Hirosawa, Wako, Saitama, 351-0198, Japan. Tel: +81-48-462-1293, Fax: +81-48-462-1290, Email: shin@riken.jp.

and their subsets have been thoroughly studied in connection with research on classical differential geometry and singularity theory (Koenderink, 1990; Belyaev et al., 1997; Cazals and Pouget, 2004b, 2005), and they were frequently used for shape interrogation purposes (see, for example, (Hosaka, 1992, Sect. 7.4), (Hallinan et al., 1999, Chap. 6), (Porteous, 1994, Chap. 11), and references therein). Also numerous applications in image and data analysis (Monga et al., 1992), quality control of free-form surfaces (Hosaka, 1992), human perception (Hoffman and Richards, 1985), analysis and registration of anatomical structures (Pennec et al., 2000), geomorphology (Little and Shi, 2001), and non-photorealistic rendering (Interrante et al., 1995; DeCarlo et al., 2003) have been proposed. The so-called *crest lines* (Thirion et al., 1992) are formed by the perceptually salient ridge points and consist of the surface points where the magnitude of the largest (in absolute value) principal curvature attains a maximum along its corresponding line of curvature. The ridges possess many interesting properties. In particular, they can be defined as the loci of surface points where the osculating spheres have high-order contacts with the surface and, therefore, the ridges are invariant under inversion of the surface w.r.t. any sphere (Porteous, 1987). The ridges can be also described as the surface curves corresponding to the cuspidal edges of the two focal surfaces (Porteous, 1994, Chap. 11).

Practical detection of the crest lines and other types of the principal curvature extrema is a difficult computational task because it requires a high-quality estimation of the principal curvature tensor and curvature derivatives. In general, global fitting methods are supposed to do a better job in estimating high-order surface derivatives and, therefore, to allow for achieving more accurate detection of surface curvature features (Kent et al., 1996; Ohtake et al., 2004) than local estimation schemes. On the other hand, the local schemes are much faster and often demonstrate a quite satisfactory performance (Guéziec, 1993; Stylianou and Farin, 2004; Cazals and Pouget, 2004a).

The vast majority of the local schemes for detecting the crest lines can be separated into those based on local polynomial fitting (Cazals et al., 2006a,b; Kim and Kim, 2006; Yoshizawa et al., 2005) and schemes based on discrete differential operators (Hildebrandt et al., 2005). While estimating surface curvatures and their derivatives with geometrically inspired discrete differential operators (Hildebrandt et al., 2005; Rusinkiewicz, 2004; Yoshizawa et al., 2007) is more elegant than using fitting methods. The former usually requires noise elimination and the latter seems more robust. On the other hand, as pointed out in (Rusinkiewicz, 2004), fitting methods incorporate a certain amount of smoothing in the curvature and curvature derivative estimation processes and that amount is very difficult to control. Another limitation of fitting schemes consists of their relatively low speed to compare with discrete differential operators. Further, since predefined local primitives are used for fitting, one cannot expect a truly faithful estimation of surface differential properties.

Our geometry-based finite difference method (Yoshizawa et al., 2007) exploits geometric relationships between a given surface and its focal surfaces, namely between the derivatives of the principal curvatures along their corresponding curvature lines and the area elements of the focal surfaces. The idea to use properties of focal surfaces for detecting principal curvature extrema was previously considered in (Lukács and Andor, 1998) and (Watanabe and Belyaev, 2001). To compare with these previous works where only basic qualitative connections between geometries of the surface and its focal set were considered, a deeper quantitative understanding of the relationships was used (Yoshizawa et al., 2007).

Our contribution. In this paper, we revise, enhance, and test three recent techniques for detecting and drawing the crest lines on surfaces approximated by dense triangle meshes:

(a) the local polynomial fitting scheme of (Yoshizawa et al., 2005);
(b) an adapted and modified version of the general finite-difference curvature tensor fitting approach of (Rusinkiewicz, 2004);
(c) the focal surface based technique of (Yoshizawa et al., 2007).

Our general procedure consists of three phases:

(1) estimating the principal curvature tensor and curvature derivatives,
(2) tracing the crest lines, and
(3) efficient thresholding of the lines.

For the first phase, we use a new focal surface based finite difference scheme (Yoshizawa et al., 2007) and appropriately modified versions of a local polynomial fitting scheme of (Goldfeather and Interrante, 2004) and a curvature tensor fitting scheme of (Rusinkiewicz, 2004). For the second phase, we develop and use an enhancement of the zero-crossing curvature-extremum detection procedure of (Ohtake et al., 2004). Our crest line thresholding strategy consists of penalizing the crest line points in surface regions close to Dupin's cyclide patches (every point of a Dupin's cyclide is a ridge point and, therefore, the crest lines are not defined properly there). Finally we consider applications of the crest lines to adaptive mesh simplification.

While (c) demonstrates the fastest performance and delivers very good results for dense noise-free meshes, (a) achieves the highest accuracy among the approaches, The tensor fitting approach (b) occupies an intermediate position between (a) and (c). It is worth to mention here that (c) is a pure geometrical and without a doubt has a greater mathematical elegance then (a) and (b).

Paper organization. The three approaches we present in this paper use the same zero-crossing curvature-extremum detection procedure (Ohtake et al., 2004), the same procedure for tracing the detected crest lines (Yoshizawa et al., 2005), and very similar thresholding/filtering schemes. So we do not describe the approaches separately. In Section 2 we present a collection of mathematical results needed for (a), (b), and (c). Section 3 describes curvature and curvature extremality estimation schemes corresponding to the approaches. Sections 4 and 5 are devoted to the crest line tracing and thresholding stages, respectively. In Section 6 we consider an application of crest lines to feature preserving mesh decimation. We compare the approaches, reveal their strong and week sides, and conclude in Section 7.

2 Differential Geometry Background

Crest lines, ridges, focal surfaces, and Dupin cyclides. Consider a smooth oriented surface $\mathcal{S}$ given by radius-vector $\mathbf{r}$ and denote by $k_{\max}$ and $k_{\min}$ its maximal and minimal principal curvatures, $k_{\max} \geq k_{\min}$. Let $\mathbf{t}_{\max}$ and $\mathbf{t}_{\min}$ be the corresponding principal directions. Denote by $e_{\max}$ and $e_{\min}$ the derivatives of the principal curvatures along their corresponding curvatures directions:

$$e_{\max} = \partial k_{\max}/\partial \mathbf{t}_{\max}, \qquad e_{\min} = \partial k_{\min}/\partial \mathbf{t}_{\min}. \tag{1}$$

Following (Thirion, 1996) we call $e_{\max}$ and $e_{\min}$ the *extremality coefficients*. Strictly speaking, the extremality coefficients are not defined at the umbilical points (the points where $k_{\max} = k_{\min}$) since the principal directions are undefined there. The ridges are formed by the closure of points on $\mathcal{S}$ where one of the extremality coefficients vanishes. According to this definition, the umbilical points can be considered as ridge points. In (Porteous, 1994; Hallinan et al., 1999) the ridge patterns in small vicinities of umbilical points are analyzed.

The crest lines consist of perceptually salient ridge points. We distinguish convex and concave crest lines. The convex crest lines are given by

$$e_{\max} = 0, \quad \partial e_{\max}/\partial \mathbf{t}_{\max} < 0, \quad k_{\max} > |k_{\min}|,$$

while the concave crest lines are characterized by

$$e_{\min} = 0, \quad \partial e_{\min}/\partial \mathbf{t}_{\min} > 0, \quad k_{\min} < -|k_{\max}|.$$

The convex and concave crest lines are dual w.r.t. the surface orientation: changing the orientation turns the convex crest lines into concave one and vice versa.

Denote by $\mathcal{F}$ the focal set of $\mathcal{S}$. The focal set is formed by the principal centers of curvature and consists of two focal surfaces corresponding to the maximal and minimal principal curvatures

$$\mathbf{f}_{\max} = \mathbf{r} + \mathbf{n}/k_{\max} \quad \text{and} \quad \mathbf{f}_{\min} = \mathbf{r} + \mathbf{n}/k_{\min}.$$

The focal surfaces $\mathbf{f}_{\max}$ and $\mathbf{f}_{\min}$ have singularities which, in the generic case, consist of cuspidal edges, space curves corresponding to the ridges on $\mathcal{S}$, and isolated point singularities (Figure 1 demonstrate the focal surfaces of an ellipsoid).

The crest lines form a subset of the ridges and correspond to certain parts of the cuspidal edges of the focal surfaces. The ridges and, therefore, the crest lines are not defined properly on the Dupin cyclides, special surfaces which can be characterized by the condition that both their focal surfaces degenerate into space curves (Eisenhart, 1909, §132). The Dupin cyclides were introduced by French geometer Charles Dupin at the beginning of the 19th century and since then have been intensively studied in connection with various shape modeling tasks (see, for example, (Chandru et al., 1989), (Foufou and Garnier, 2004), and references therein). Figure 2 shows typical Dupin cyclides.

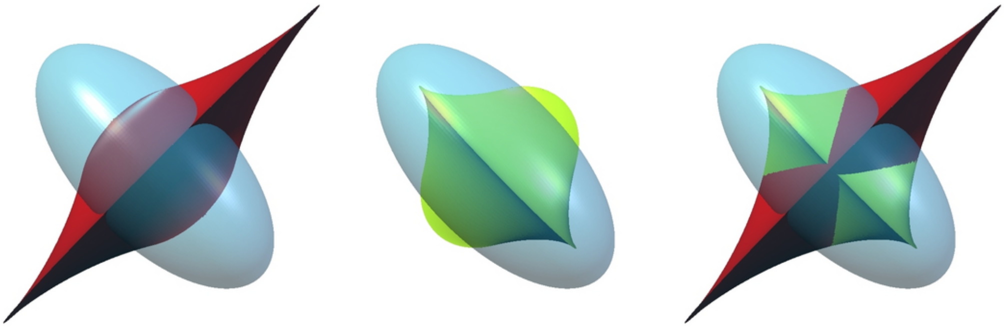

Figure 1. The focal surfaces of an ellipsoid.

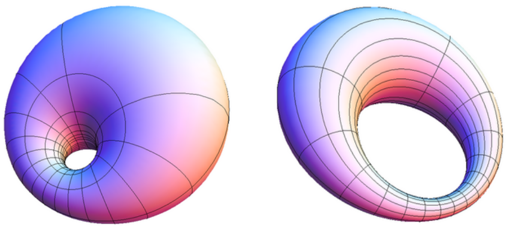

Figure 2. Dupin cyclides - surfaces without ridges.

One can show that the Dupin cyclides are characterized by the condition

$$e_{\max} = 0 = e_{\min} \quad \text{or, equivalently,} \quad |e_{\max}|^2 + |e_{\min}|^2 = 0. \tag{2}$$

Notice that the left-hand side of right-most equation in (2) is the integrand of the so-called MVS functional introduced in (Moreton and Séquin, 1992) for fair surface design purposes.

There are interesting relations between the extremality coefficients $e_{\max}$ and $e_{\min}$ and area elements of the two focal surfaces $\mathbf{f}_{\max}$ and $\mathbf{f}_{\min}$. Namely, let $\mathbf{n}_{\max}$ and $\mathbf{n}_{\min}$ be the orientation normals of $\mathbf{f}_{\max}$ and $\mathbf{f}_{\min}$, respectively. Denote by $D_{\max}\mathbf{n}_{\max}$ and $D_{\min}\mathbf{n}_{\min}$ form the oriented area elements of $\mathbf{f}_{\max}$ and $\mathbf{f}_{\min}$ (i.e., $D_{\max}$ and $D_{\min}$ are the determinants of the 2×2 matrices composed of the coefficients of the first fundamental forms of $\mathbf{f}_{\max}$ and $\mathbf{f}_{\min}$), respectively. Then

$$e_{\max}\mathbf{t}_{\max} = \frac{k_{\max}^3 D_{\max}}{k_{\max} - k_{\min}}\mathbf{n}_{\max}, \quad e_{\min}\mathbf{t}_{\min} = \frac{k_{\min}^3 D_{\min}}{k_{\min} - k_{\max}}\mathbf{n}_{\min}. \tag{3}$$

It is worth to observe that (3) implies simple relations between the surface principal directions $\mathbf{t}_{\max}$, $\mathbf{t}_{\min}$ and normals $\mathbf{n}_{\max}$, $\mathbf{n}_{\min}$ of the focal surfaces $\mathbf{f}_{\max}$, $\mathbf{f}_{\min}$. The relations were recently used as key ingredients of a novel approach to robust estimating the principal directions and curvatures of triangulated surfaces (Yu et al., 2007).

A proof of (3) can be found, for example, in (Weatherburn, 1927, §75). Below we give our own simple proof of these formulas. In a small vicinity of non-umbilical point of $\mathcal{S}$ let us consider the lines of curvature parameterized by their arc lengths. Then the surface is locally represented in parametric form $\mathbf{r} = \mathbf{r}(u, v)$ for which

$$\mathbf{r}_u = \mathbf{t}_{\max}, \qquad \mathbf{r}_v = \mathbf{t}_{\min}, \qquad \mathbf{n}_u = -k_{\max}\mathbf{t}_{\max}, \qquad \mathbf{n}_v = -k_{\min}\mathbf{t}_{\min}.$$

Consider now a generalized focal surface

$$\mathbf{f} = \mathbf{r}(u, v) + R(u, v)\mathbf{n}(u, v). \tag{4}$$

Substitutions $R = R_{\max} \equiv 1/k_{\max}$ and $R = R_{\min} \equiv 1/k_{\min}$ give us the standard focal surfaces $\mathbf{f}_{\max}$ and $\mathbf{f}_{\min}$, respectively. The oriented area element $\mathbf{f}_u \times \mathbf{f}_v$ of (4) is

$$-R_u\left(1 - R/R_{\min}\right)\mathbf{t}_{\max} - R_v\left(1 - R/R_{\max}\right)\mathbf{t}_{\min} + \left(1 - R/R_{\max}\right)\left(1 - R/R_{\min}\right)\mathbf{n}$$

and (3) immediately follows.

Formulas (3) explain the “focusing” effect of each focal surface near its edges of regression: the area element of a focal surface degenerates to zero at the edges of regression. This observation was used in (Lukács and Andor, 1998; Watanabe and Belyaev, 2001) for detecting creases on meshes. In our study, we employ the full power of (3).

Principal curvatures and their gradients from surface Laplacian. It is widely known that

$$\Delta_S \mathbf{r} = \left(k_{\max} + k_{\min}\right)\mathbf{n}, \tag{5}$$

where $\mathbf{n}$ is the orientation normal for a smooth surface $\mathbf{r}$ and Δ_S is the Laplace-Beltrami operator (the surface Laplacian). It is much less known that

$$\Delta_S \mathbf{n} = -\left(k_{\max}^2 + k_{\min}^2\right)\mathbf{n} - \nabla_S\left(k_{\max} + k_{\min}\right), \tag{6}$$

where ∇_S stands for the surface tangential gradient operator. A proof of (6) can be found in classical differential geometry textbook (Weatherburn, 1927, §119) whose author considered this formula as a key ingredient of his surface vector analysis approach (Weatherburn, 1930).

Given a good approximation of the normal $\mathbf{n}$ and Laplace-Beltrami operator Δ_S for a surface approximated by a mesh, one can estimate the principal curvature tensor and the surface gradients of the principal curvatures as follows. Note that (5) and (6) imply

$$\Delta_S \mathbf{r} \cdot \mathbf{n} = k_{\max} + k_{\min}, \qquad \Delta_S \mathbf{n} \cdot \mathbf{n} = -\left(k_{\max}^2 + k_{\min}^2\right) \tag{7}$$

and the principal curvatures are determined directly from (7). Now one can build meshes approximating the focal surfaces and use (3) to estimate the principal directions and extremality coefficients. Finally, if necessary, the remaining derivatives of the principal curvatures can be estimated from (6).

Curvature extremalities for implicit surfaces. It seems well known that for a surface given in implicit form $F(\mathbf{x}) = 0$, $\mathbf{x} = (x_1, x_2, x_3)$, extremailty coefficient $e = \partial k / \partial \mathbf{t}$ is given by

$$e = \nabla k \cdot \mathbf{t} = \frac{F_{ijl} t_i t_j t_l + 3k F_{ij} t_i n_j}{|\nabla F|}, \tag{8}$$

where F_{ij} and F_{ijl} denote the second and third partial derivatives of $F(\mathbf{x})$, respectively, $\mathbf{t} = (t_1, t_2, t_3)$ is the principal direction corresponding to a principal curvature k, $\mathbf{n} = (n_1, n_2, n_3)$ is the unit surface normal, and the summation over repeated indices is implied. In its present from, (8) is derived in (Belyaev et al., 1998). See, for example, (Porteous, 1994, Exercise 11.8) and also (Monga et al., 1992) where a small mistake in the final formulas for the curvature derivatives is made.

Assume now that the coordinates are chosen such that the origin of coordinates is situated on the surface and the coordinate vectors coincide with the frame $\mathbf{t}_{\max}$, $\mathbf{t}_{\min}$, and $\mathbf{n}$. Then our surface $\mathcal{S}$ is given locally in the Monge form $z = h(x, y)$ with

$$\begin{aligned} h(x,y) = {} & \frac{1}{2}(b_0 x^2 + 2b_1 xy + b_2 y^2) + \frac{1}{6}(c_0 x^3 + 3c_1 x^2 y + 3c_2 x y^2 + c_3 y^3) \\ & + \frac{1}{24}(d_0 x^4 + 4d_1 x^3 y + 6d_2 x^2 y^2 + 4d_3 x y^3 + d_4 y^4) + \dots . \end{aligned} \tag{9}$$

Straightforward computations show that, in this particular case, (8) simplifies into

$$e = \partial k / \partial \mathbf{t} = F_{ijl} t_i t_j t_l, \tag{10}$$

where, as before, the summation over repeated indices is assumed. Now (9) and (10) give

$$e = \partial k/\partial \mathbf{t} = \begin{pmatrix} t_1^2 \\ t_2^2 \end{pmatrix}^T \begin{pmatrix} c_0 & c_1 \\ c_2 & c_3 \end{pmatrix} \begin{pmatrix} t_1 \\ t_2 \end{pmatrix} \tag{11}$$

at the local origin $h(0,0)$ where $\mathbf{t} = (t_1, t_2)$ is the principal direction corresponding to principal curvature k.

It is interesting to compare (11) with the derivative-of-curvature tensor

$$\mathbf{C} = \left(\begin{pmatrix} a & b \\ b & c \end{pmatrix} \begin{pmatrix} b & c \\ c & d \end{pmatrix} \right) \tag{12}$$

derived in (Rusinkiewicz, 2004) (see formula (8) there). The derivative of curvature in direction $\mathbf{t}$ is given by

$$\mathbf{C}(\mathbf{t}, \mathbf{t}, \mathbf{t}) = \begin{pmatrix} t_1^2 \\ t_2^2 \end{pmatrix}^T \begin{pmatrix} a & 3b \\ 3c & d \end{pmatrix} \begin{pmatrix} t_1 \\ t_2 \end{pmatrix} \tag{13}$$

which is equivalent to (11) with $c_0 = a$, $c_1 = 3b$, $c_2 = 3c$, and $c_3 = d$.

Invariance properties of curvature extrema. It is not difficult to show that the ridges, the full set of the extrema of the principal curvatures along their corresponding curvature directions, are Möbius-invariant (i.e., scale-independent and inversion-invariant). Indeed, they are obviously scale-invariant and their invariance w.r.t. the inversions can be easily verified by direct computations.

Consider surface $\tilde{\mathbf{r}}$ obtained from $\mathbf{r}$ by inversion w.r.t. the sphere of radius c centered at the origin of coordinates

$$\tilde{\mathbf{r}} = c^2 \mathbf{r}/r^2, \qquad r^2 = \mathbf{r} \cdot \mathbf{r}.$$

Then the length elements of $\tilde{\mathbf{r}}$ and $\mathbf{r}$ are related by

$$d\tilde{s} = c^2 ds/r^2. \tag{14}$$

Direct computations (Weatherburn, 1927, §§82-83) show that the principal curvatures of $\tilde{\mathbf{r}}$ are given by

$$\tilde{k}_{\max} = -\frac{r^2}{c^2} k_{\max} - \frac{2}{c^2} \mathbf{r} \cdot \mathbf{n}, \qquad \tilde{k}_{\min} = -\frac{r^2}{c^2} k_{\min} - \frac{2}{c^2} \mathbf{r} \cdot \mathbf{n} \tag{15}$$

and the curvature lines of $\mathbf{r}$ are mapped onto the curvature lines of $\tilde{\mathbf{r}}$. One can observe that (14) and (15) imply the Möbius-invariance of the differential form

$$(k_{\max} - k_{\min})^2 dA$$

corresponding to the well-known Willmore energy (Willmore, 2000). The Willmore energy measures deviation from sphericity and is currently a subject of intensive research in differential geometry (Hertrich-Jeromin, 2003) and geometric modeling (Bobenko and Schröder, 2005); see also references therein.

Now differentiating $\tilde{k}_{\max}$ and $\tilde{k}_{\min}$ in (15) along their corresponding curvature lines and using the Rodrigues' curvature formula gives a new and unexpected result

$$\frac{c^2}{r^2}\tilde{e}_{\max} = \frac{\partial \tilde{k}_{\max}}{\partial \mathbf{t}_{\max}} = -\frac{r^2}{c^2} e_{\max}, \qquad \frac{c^2}{r^2}\tilde{e}_{\min} = \frac{\partial \tilde{k}_{\min}}{\partial \mathbf{t}_{\min}} = -\frac{r^2}{c^2} e_{\min} \tag{16}$$

and the inversion-invariance of the ridges follows.

Using (16) we arrive at

$$\tilde{e}_{\max} d\tilde{s}^2 = -e_{\max} ds^2, \quad \tilde{e}_{\min} d\tilde{s}^2 = -e_{\min} ds^2 \tag{17}$$

and can easily construct a number of Möbius-invariant differential forms:

$$\sqrt{|e_{\max}| + |e_{\min}|}\, ds, \tag{18}$$

$$\sqrt{e_{\max}^2 + e_{\min}^2}\, dA, \quad \sqrt{|e_{\max} e_{\min}|}\, dA, \quad |e_{\max}| dA, \quad |e_{\min}| dA, \tag{19}$$

$$\frac{e_{\max}^2\, dA}{(k_{\max} - k_{\min})^2}, \quad \frac{e_{\min}^2\, dA}{(k_{\max} - k_{\min})^2}, \quad \frac{e_{\max} e_{\min}\, dA}{(k_{\max} - k_{\min})^2}, \tag{20}$$

where ds and dA are curve-on-surface arc-length and surface area elements, respectively.

Some of these Möbius-invariant surface-based differential forms were studied before. For example, in (Ferapontov, 2000) it was shown that the last term of (20) is also offset-invariant, i.e. invariant w.r.t shifting each surface point to a fixed distance along the surface normal direction at that point. Some others seem to be new although they can be obtained from a complete Möbius invariant system derived in (Wang, 1992).

It is worth to notice a similarity between the Möbius-invariant surface energy

$$\iint \sqrt{e_{\max}^2 + e_{\min}^2}\, dA$$

corresponding to the first differential form in (19) and the MVS functionals

$$\iint \left(e_{\max}^2 + e_{\min}^2\right) dA \quad \text{and} \quad \iint \left(e_{\max}^2 + e_{\min}^2\right) dA \cdot \iint dA$$

introduced and studied in (Moreton and Séquin, 1992; Joshi and Séquin, 2007).

In our study, we will use (18) for selecting perceptually salient subsets of the crest lines.

3 Practical Estimation of Surface Curvatures and Curvature Extremalities

Given a triangle mesh $\mathcal{M}$ approximating a smooth surface $\mathcal{S}$, our first task is to get an accurate and robust estimation of the surface normal. Our numerical experiments suggest that a simple method of (Max, 1999) is a very good choice.

Since the curvature extrema are very sensitive to even small shape variations, it is a good idea to apply first a simple parameter-free smoothing procedure. As we will see later, it is not really necessary but leads to more visually pleasant patterns of the crest lines. Namely, motivated by (Taubin, 2002), we consider the dual mesh consisting of the triangle centroids of $\mathcal{M}$ and construct an auxiliary mesh whose vertices are the centroids of the polygons composing the dual mesh. The auxiliary mesh inherits the connectivity of $\mathcal{M}$.

The principal curvatures, principal directions, and the curvature extremalities are estimated at the auxiliary mesh vertices via one of the following three schemes: local cubic polynomial fitting (Yoshizawa et al., 2005), a modified version of the tensor fitting procedure of (Rusinkiewicz, 2004), and the focal surface based finite difference scheme (Yoshizawa et al., 2007). Then the crest lines are traced on $\mathcal{M}$ by using the corresponding curvature tensor and extremality coefficients of the auxiliary mesh.

Local cubic polynomial fitting. In our numerical experiments we use an enhanced version of the adjacent-normal cubic approximation method of (Goldfeather and Interrante, 2004). The cubic polynomial given by the right-hand side of (9) is fitted in the least-square sense (Goldfeather and Interrante, 2004) to each auxiliary mesh vertex and a set of its neighboring vertices. That set of neighbors is obtained from the k-ring neighborhood ($k = 1, 2, 3, 4$) of the auxiliary mesh vertex by removing those vertices whose normals make obtuse angles with the normal at the auxiliary mesh vertex.

Then the curvature tensor and extremality coefficients are derived using (9) and (11). Finally these curvature attributes are assigned to the original vertices of mesh $\mathcal{M}$.

Figure 3 compares the sets of crest lines detected on a 3D text mesh via the straightforward polynomial fitting (the top image) and the enhanced adjacent-normal cubic approximation method (we use one-ring neighborhood in this example).

Although our scheme for estimating surface derivatives seems complicated, it leads to highly effective crest line detection procedure which only slightly depends on the mesh connectivity and triangle aspect ratios. Figure 4 shows crest line patterns found on simple and complex geometrical models for various values of a user-specified parameter which controls the strength of detected crest lines.

In Figure 5 we compare the patterns of the crest lines detected on the original Stanford bunny mesh and on the mesh obtained via an implicitization of the bunny model and then polygonizing it using (Bloomenthal, 1994). Despite the fact that the new bunny mesh contains many sliver triangles and has irregular connectivity, the patterns of the crest lines found on the meshes are remarkably similar.

Figure 3. Crest lines detected on 3D text. Top: polynomial fit without preliminary estimation of mesh normals is used. Bottom: the enhanced adjacent-normal cubic approximation method is employed for estimating surface curvatures and their derivatives.

Curvature tensor fitting scheme. We use a simple modification of the scheme of (Rusinkiewicz, 2004) for estimating $e_{\max}$ and $e_{\min}$. First we use the scheme to estimate the principal curvatures and principal directions. Next we transform the coordinate system so that the axes in the tangent plane coincide with the surface principal directions and, therefore, (9) simplifies into

$$h(x, y) = \frac{1}{2}(k_{\max}x^2 + k_{\min}y^2) + \frac{1}{6}(\tilde{c}_0x^3 + 3\tilde{c}_1x^2y + 3\tilde{c}_2xy^2 + \tilde{c}_3y^3) + \dots, \quad (21)$$

where straightforward computations give

$$e_{\max} = \tilde{c}_0 \quad \text{and} \quad e_{\min} = \tilde{c}_3. \quad (22)$$

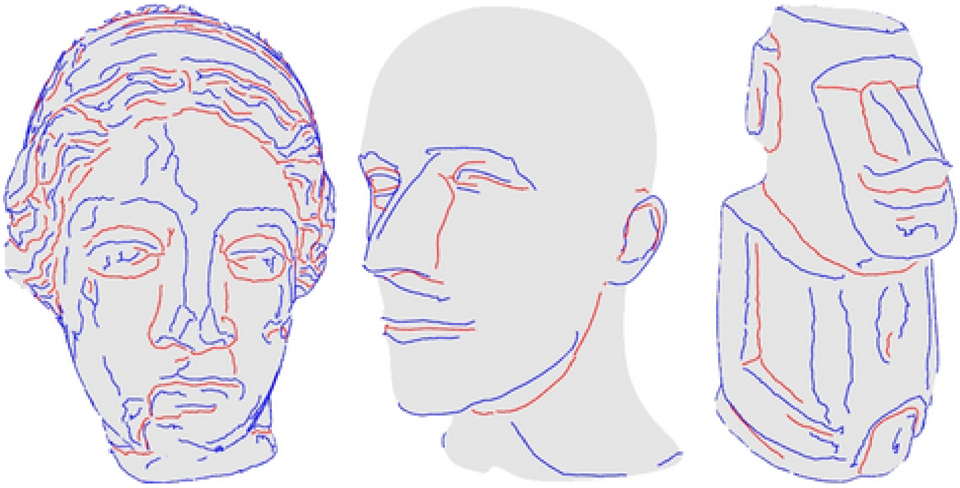

Figure 4. Crest lines detected on various triangle meshes. A scale-independent parameter T_2 of (24) is used to keep the most visually important features. For all the model one-ring neighborhood polynomial fitting is used for estimating the curvature tensor and extremalities.

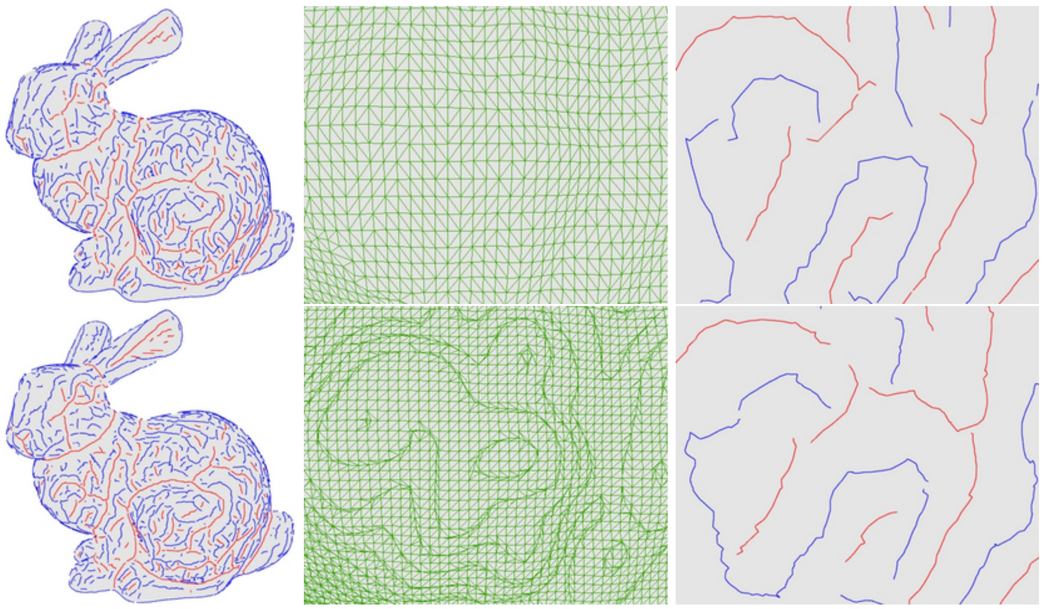

Figure 5. Patterns of crest lines and mesh triangles for two bunny models. Top: original Stanford bunny mesh with 69,451 triangles is used. Bottom: another bunny mesh with 279,984 triangles is used. The necessary surface derivatives are estimated via the enhanced cubic polynomial fitting with one-ring neighborhood for the original Stanford bunny mesh and three-ring neighborhoods for the remeshed bunny since the latter is more than three times bigger than the original one.

Then the derivative-of-curvature tensor (12) is computed. Finally, taking into account (11), (13), (21), and (22) we arrive at $e_{\max} = a$ and $e_{\min} = d$ where a and b are defined in (12). In our numerical experiments, we use program codes accompanying (Rusinkiewicz, 2004).

Focal surface based finite difference scheme. Once the normals at the auxiliary mesh vertices are estimated, the discrete principal curvatures are obtained from (7) where the standard cotan formula (Pinkall and Polthier, 1993; Meyer et al., 2003) is used to approximate the Laplace-Beltrami operator.

Now we are ready to build meshes $\mathcal{F}_{\max}, \mathcal{F}_{\min}$, discrete counterparts of the focal surfaces $\mathbf{f}_{\max}, \mathbf{f}_{\min}$, and estimate the principal directions $\mathbf{t}_{\max}, \mathbf{t}_{\min}$ and extremalities $e_{\max}, e_{\min}$ via (3). The discrete focal meshes $\mathcal{F}_{\max}$ and $\mathcal{F}_{\min}$ for the auxiliary mesh are built and their normals $\mathbf{n}_{\max}$ and $\mathbf{n}_{\min}$ are computed according to (Max, 1999).

In practice, if $|k_{\max}| > |k_{\min}|$ we set $\mathbf{t}_{\max} = \mathbf{n}_{\max}$ and $\mathbf{t}_{\min} = \mathbf{n} \times \mathbf{n}_{\max}$. Otherwise, $\mathbf{t}_{\min} = \mathbf{n}_{\min}$ and $\mathbf{t}_{\max} = \mathbf{n}_{\min} \times \mathbf{n}$.

The oriented area element at a vertex $\mathbf{v}$ of $\mathcal{F}_{\max}$ ($\mathcal{F}_{\min}$) is obtained by averaging the oriented areas of adjacent triangles. Namely, only those triangles $(\mathbf{v}, \mathbf{v}_i, \mathbf{v}_{i+1})$ from the 1-ring neighborhood of $\mathbf{v}$ contribute to the oriented area element at $\mathbf{v}$, for which $k_{\max}$ ($k_{\min}$) has the same sign at the corresponding vertices of $\mathcal{M}$. We use this curvature sign restriction condition in order to avoid troubles with the parabolic lines on $\mathbf{r}$ where the corresponding focal surfaces go to infinity. Although according to their mathematical definition, the crest lines stay aside of their corresponding parabolic lines, the above condition contributes to numerical stability of our approach. Figure 9 demonstrates the resulting crest lines via our focal surface based finite difference scheme.

4 Tracing Crest Lines

Once the principal curvature tensor and extremality coefficients are estimated at each vertex of $\mathcal{M}$, we inspect the edges of $\mathcal{M}$ and check whether they contain curvature maxima and minima. We detect the crest line vertices and connect them together following the procedure proposed in (Ohtake et al., 2004) with one small, but important, addition. It turns out that the procedure may generate several close disconnected crest lines in situations similar to those shown in the left images of Figures 6 and 7. In order to reduce the fragmentation of the crest lines we inspect the mesh vertices and their one-ring neighborhoods. For each one-ring vertex neighborhood containing crest line end-points we connect two end-points if $\alpha \leq \pi/3$, $\beta \leq \pi/3$, $\gamma \leq \pi/2$, where α, β, and γ are the angles between the end-segments and the segment connecting the end-points, as seen the right image of Figure 6. Figure 7 demonstrates how well our additional procedure of connecting the close disconnected crest lines improves the zero-crossing detection procedure of (Ohtake et al., 2004).

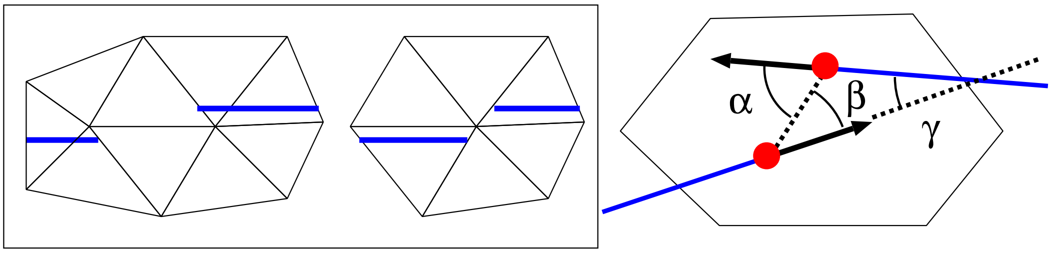

Figure 6. Left: situations when we may want to connect the crest lines (shown in bold) together. Right: angles α, β, and γ generated by crest line end-segments and the segment connecting crest line end-points are used to measure when gap-jumping is necessary.

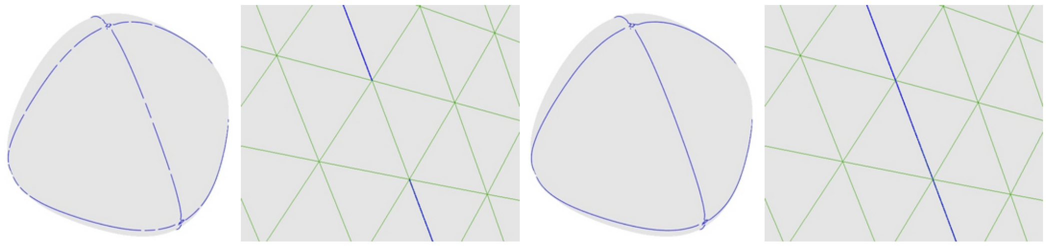

Figure 7. Gap-jumping example. Left: several close disconnected crest lines are obtained by (Ohtake et al., 2004) where the mesh edge is closely parallel to the crest lines. Right: the fragmentation is reduced by our connecting scheme.

5 Thresholding Crest Lines

After the full set of crest lines is extracted, we need a filtering procedure in order to remove spurious lines and select the most perceptually-salient crest line structures. Our motivation behind filtering the crest lines is as follows. The crest lines are a subset of the ridges which correspond to the cuspidal edges of the focal surfaces. As mentioned in Section 2, the ridges and, therefore, the crest lines are not defined properly on the Dupin cyclides. Thus we can expect that surface regions close to Dupin cyclide patches contain a noisy pattern of crest lines. The quantities

$$C_1 = |e_{\max}| + |e_{\min}| \quad \text{or} \quad C_2 = \sqrt{|e_{\max}|^2 + |e_{\min}|^2} \tag{23}$$

computed at a given surface point indicate how far/close a small surface neighborhood around the point is from being a part of a Dupin cyclide. Thus the local cyclidities (23) can be used to filter out insignificant crest lines arising at mesh parts corresponding to planar, spherical, conical, cylindrical, and other Dupin cyclide regions on a smooth surface.

Cyclidity measures. We use two cyclidity thresholds to measure the strengths of the detecting crest lines:

$$T_1 = \int \sqrt{|e_{\max}| + |e_{\min}|}\, ds \quad \text{and} \quad T_2 = \int ds \cdot \int \sqrt{|e_{\max}|^2 + |e_{\min}|^2}\, ds. \tag{24}$$

Both these cyclidity measures are scale-independent. In addition, as shown in Section 2, the first one is Möbius-invariant.

Cyclidity thresholds (24) involve third-order surface derivatives and, therefore, are more complex than the thresholding scheme used in (Ohtake et al., 2004) where the integral of a principal curvature along a feature line was used. On the other hand, filtering crest lines with either of the cyclidity thresholds of (24) is simpler than the thresholding scheme proposed in (Cazals and Pouget, 2004a) where a second-order curvature derivative is used for removing spurious and insignificant ridges and crest lines.

We use a linear interpolation scheme for estimating the local cyclidities C_1 and C_2 at crest line vertex $\mathbf{v}$ located on mesh edge $[\mathbf{p}, \mathbf{q}]$:

$$C(\mathbf{v}) = \frac{a\,C(\mathbf{p}) + b\,C(\mathbf{q})}{a+b},$$

where $a = |e_{\max}(\mathbf{q})|$, $b = |e_{\max}(\mathbf{p})|$ for the convex crest lines and $a = |e_{\min}(\mathbf{q})|$, $b = |e_{\min}(\mathbf{p})|$ for the concave ones. Now the integrals in (24) are estimated by a simple trapezoid approximation similar to that used in (Ohtake et al., 2004).

Figure 8 demonstrates how filtering with T_1 works for a model with flat and cylindrical regions. Notice how well the crest lines detected at the mesh parts approximating those regions are filtered out by increasing T_1. Figure 9 provides with more examples of filtering the crest lines using the cyclidity-based measure T_1.

Figure 10 demonstrates how our cyclidity-based filtering schemes work for a model with spherical and cylindrical regions. In this particular example, filtering with T_2 was applied. The use of T_1 produces very similar results. Figure 11 exposes crest lines detected on a more complex model containing flat and cylindrical regions. Increasing T_2 allows us to remove inessential crest lines while preserving salient ones. The figure also demonstrates how the size of vertex neighborhoods used for polynomial fitting affects the crest line detection procedure. A larger neighborhood leads to smoother approximation of the mesh and, therefore, allows us to disregard the crest lines located in slightly convex/concave regions. See also Figure 4 where one-ring neighborhood polynomial fitting is used for all the models.

6 Crest Lines and Mesh Simplification

In this section, we develop a quadric-based mesh simplification procedure guided by the distance field from crest lines. Our use of crest lines for adaptive mesh simplification purposes is inspired by (Kho and Garland, 2003). Since crest lines on a mesh are important shape features, it is natural to simplify the mesh aggressively far from the most salient crest lines and preserve the mesh in a vicinity of them.

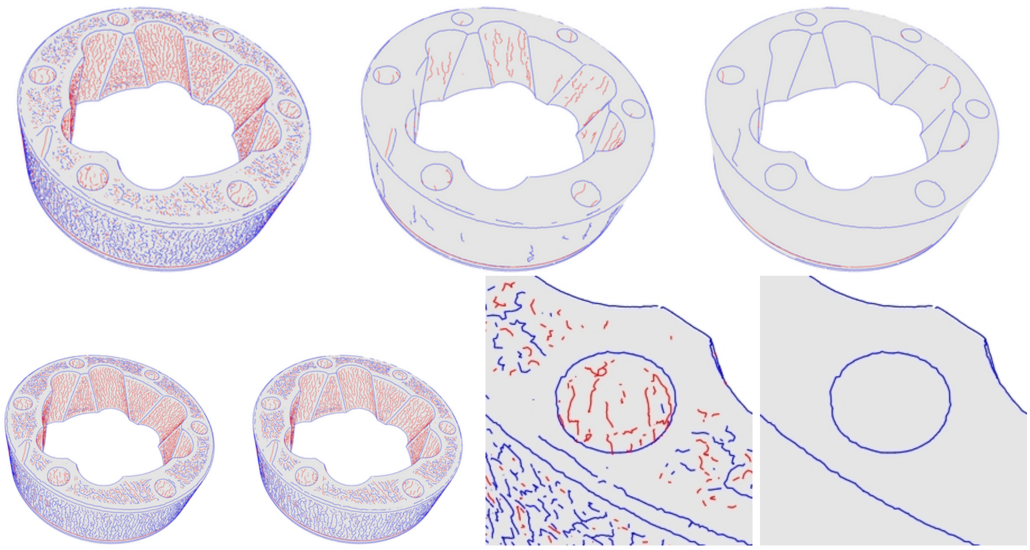

Figure 8. Top: detecting crest lines for a model containing flat and cylindrical regions for various values of threshold T_1. The focal surface based finite difference scheme is employed to estimate curvature tensor and extremalities. Note that appearance of spurious ridges does not depend on curvature estimation algorithms, see the bottom-left two images which are the crest lines generated by using the local polynomial and tensor fitting schemes, respectively.

Given a set of feature lines (crest lines, in our case) on surface $\mathcal{S}$, following (Lévy et al., 2002) for a surface point $\mathbf{p} \in \mathcal{S}$ we consider $d(\mathbf{p})$ the geodesic distance between $\mathbf{p}$ and the closest feature line (crest line) point. Let $\max(d)$ be the maximum of the geodesic distances $d(\mathbf{p})$ over all points of $\mathcal{S}$. We introduce a scale-independent weighted distance function

$$F(d) = \left(\frac{d}{\max(d)} + \epsilon \right)^{\eta}, \tag{25}$$

where ϵ is a regularization parameter (in all our experiments we use $\epsilon = 0.1$) and η is a positive user-specified parameter which is used to control a degree of influence of the crest lines.

Once the crest lines are detected and filtered, we compute a discrete feature distance d_i for each triangle $T_i \in \mathcal{M}$. Let us define the distance between two triangles T_j and T_i of $\mathcal{M}$ sharing a common edge as the sum of distances between the triangle centroids and the edge midpoint. To compute $\{d_i\}$ we use a variant of the Floyd-Warshall all-pairs shortest path algorithm.

Figure 12 visualizes the distance fields computed on the Max-Planck bust and Stanford bunny meshes.

Similar to (Kho and Garland, 2003) a weighted quadric error metric $w_j Q(T_j)$ is assigned to each triangle T_j of mesh $\mathcal{M}$, where $Q(T_j)$ is the standard Garland-Heckbert QEM (Garland and Heckbert, 1997). We set $w_j = 1/F(d_j)$ and control

Figure 9. Convex (blue) and concave (red) crest lines detected on polygonal models with many geometric features of various kinds. Center: no thresholding is applied. Right: the crest lines are filtered by using T_1. One can observe that spurious crest lines initially detected on spherical parts of the gearbox model (third from the top) are efficiently removed. Here the focal surface based finite difference scheme is employed for estimating the principal curvature tensor and extremalities.

the degree of influence of crest lines via parameter η in (25). Figure 13 presents the Max-Planck mesh its eye region 90%-decimated for various values of η. The

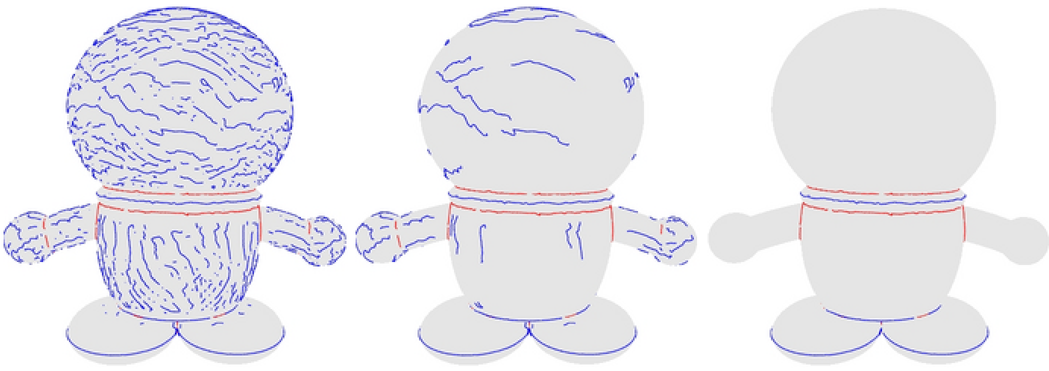

Figure 10. Detecting crest lines for a model containing spherical and cylindrical regions for various values of threshold T_2. The local polynomial fitting scheme with three-ring neighborhood is used to estimate curvature tensor and extremalities.

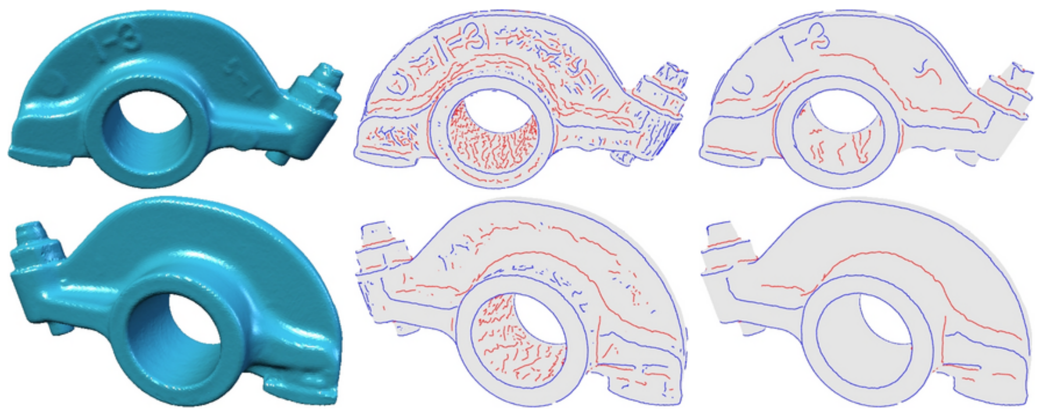

Figure 11. Crest lines detected on a mechanical part model with different values of threshold T_2. The local polynomial fitting scheme with one-ring (top) and four-ring (bottom) neighborhoods are used to estimate curvature tensor and extremalities.

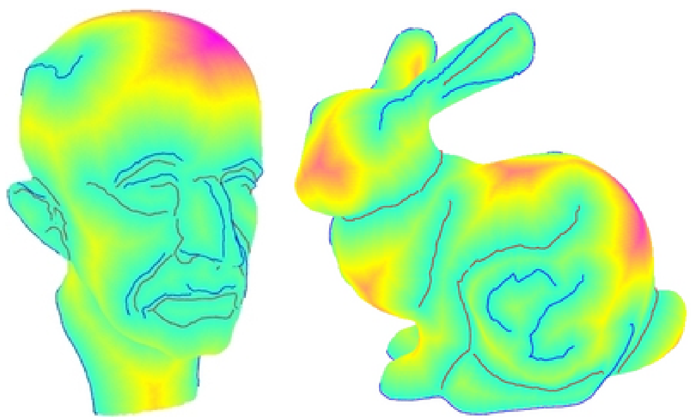

Figure 12. Distance from salient crest lines is visualized for Max-Planck bust and Stanford bunny meshes. The crest lines are found with the local polynomial fitting with three-ring neighborhood for both the models.

detected crest lines are those shown in the left image of Fig. 12. The mesh density is changing smoothly according to geodesic distance to the crest lines.

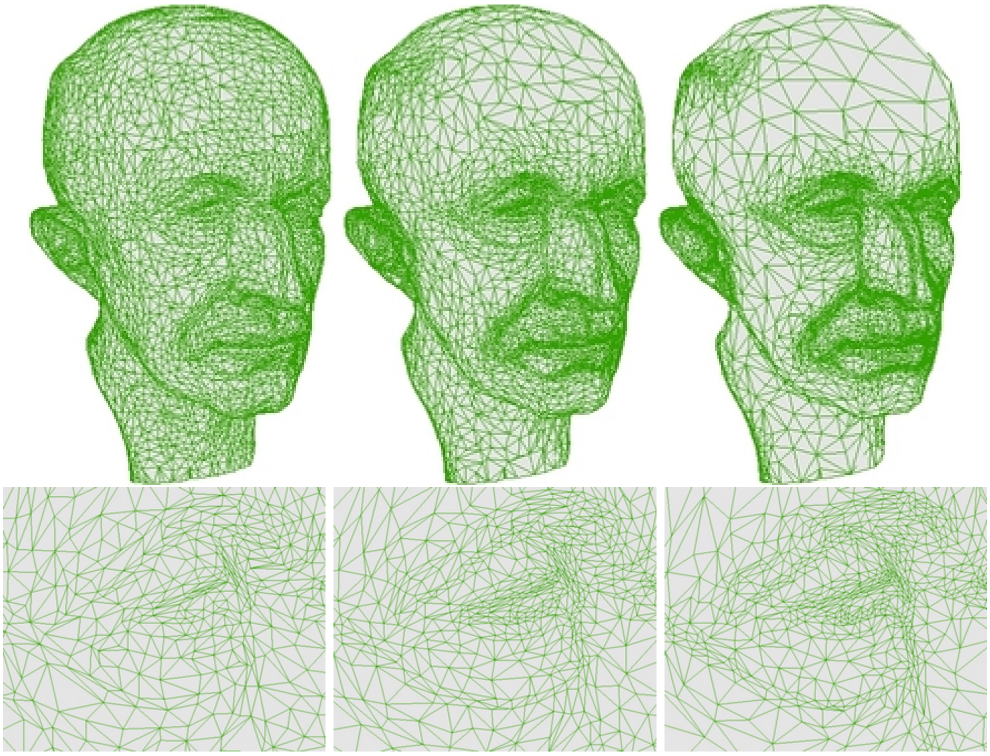

Figure 13. Max-Planck mesh and its eye part 90%-decimated for various values of η. The left image ($\eta = 0$) shows the result of the standard Garland-Heckbert decimation procedure.

7 Discussion and Conclusion

We have developed robust and reliable algorithms for detecting the crest lines on surfaces approximated by dense triangle meshes. According to our experiments [1] the crest line detection with cubic polynomial fitting achieves the speed of about 100/k thousand triangles per second if the k-ring vertex neighborhoods are used for fitting (i.e., the computational time is proportional to the size of the vertex neighborhood used for fitting). Our modification of the curvature tensor fitting scheme of (Rusinkiewicz, 2004) and the focal surface approach are much faster: they process 0.5 M and 1-1.2 M triangles per second, respectively. Note that so high speeds of the two latter methods are achieved because almost no mesh smoothing is performed during the crest line detection and tracing stages. So the first method is less

[1] A Core2Duo E6600 (2.4 GHz) PC with 2GB RAM equipped with gcc 4.1.1 C++ compiler is used. No parallelization is applied.

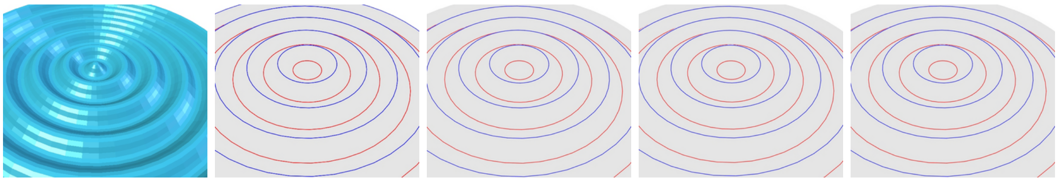

(a) (b) (c) (d) (e)

Figure 14. Comparison with the exact crest lines. (a): the input mesh generated by sampling on an analytical surface. (b): the exact crest lines. (c,d,e): our results with the local polynomial fitting (c), curvature tensor fitting (d), and focal surface based finite difference (e) schemes. The mesh we used to approximate the waving surface is not dense: it consists of less than 5K triangles only. Nevertheless the L^2 and L^∞ (max-norm) error estimates for the curvature extremality coefficients are reasonably good, see Figure 15.

sensitive to noise and produces better results for noisy data while the second and third ones deliver better results for clean data.

All the three methods are capable of achieving high quality results in detecting the crest lines to compare with schemes based on global fitting procedures. Figure 16 provides the reader with a visual quality comparison of our algorithms and one developed in (Ohtake et al., 2004) where hierarchical CS-RBF fitting was employed. Figures 14 and 15 deliver the visual and numerical comparisons of our crest line detection algorithms with the exact results obtained analytically for a trigonometric surface $\mathbf{r}(u,v) = [u\cos v, u\sin v, \cos u]$.

In addition to high speed performance, our methods demonstrate good results while processing different types of meshes, as seen in Figures 3-5, 8-11, 14, 16, and 17. Further, as demonstrated in Figures 5 and 17, our approaches are robust w.r.t. the mesh quality: the Stanford Bunny and Vase-Lion models shown in the figures have the quite irregular mesh structures. In Figure 17, we present also an example of extracting the crest lines in the case when no smoothing is applied to the mesh $\mathcal{M}$. While it delivers a truly faithful detection of the crest lines, a small amount of smoothing seems necessary to get visually pleasable results in detecting these delicate surface features.

	L^2				L^∞			
	$k_{\max}$	$k_{\min}$	$e_{\max}$	$e_{\min}$	$k_{\max}$	$k_{\min}$	$e_{\max}$	$e_{\min}$
cubic fitting	0.044	0.046	0.126	0.145	0.313	0.313	0.479	0.563
tensor fitting	0.055	0.059	0.163	0.176	0.383	0.383	0.59	0.707
focal surfaces	0.084	0.085	0.221	0.225	0.741	0.362	0.881	0.826

Figure 15. The L^2 and max-norm errors for the estimated curvature tensor and extremalities of the waving surface (see Figure 14) via the local polynomial fitting (a), curvature tensor fitting (b), and focal surface based finite difference (c) schemes.

Our focal surface approach can be naturally extended to dealing with point clouds

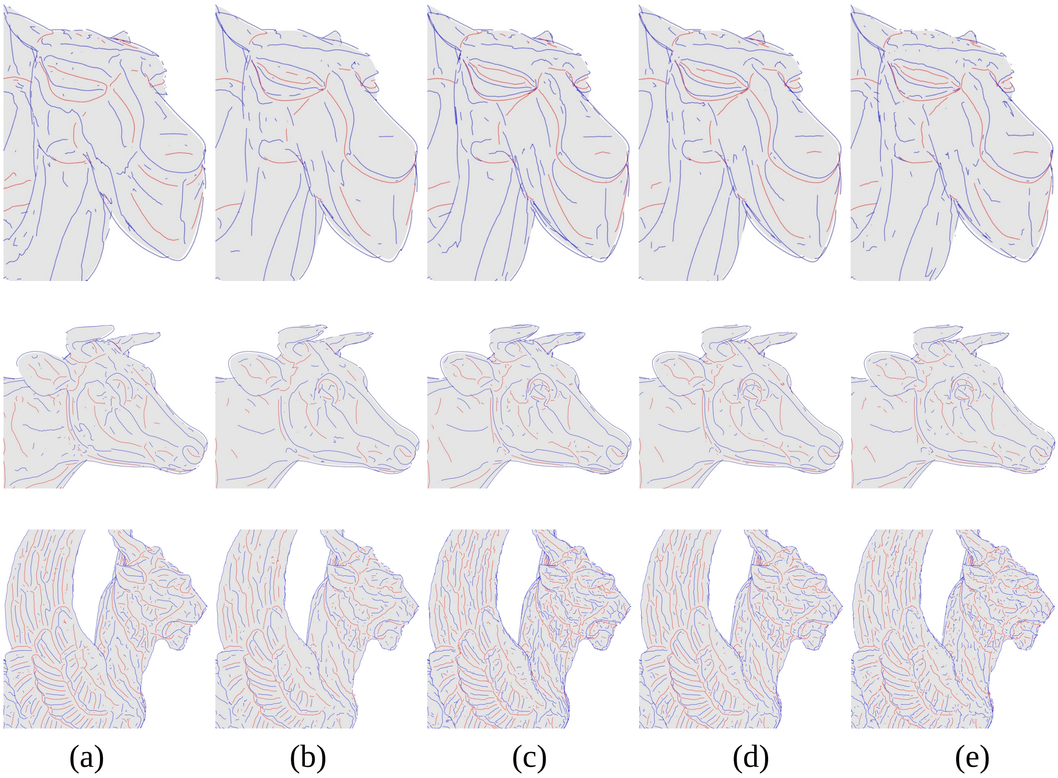

Figure 16. A comparison of crest line detection methods. The crest lines are traced on Camel (78 K triangles), Cow (93 K triangles), and Feline (399 K triangles) models, no filtering is applied. (a): Hierarchical CS-RBF fitting (Ohtake et al., 2004) (7th octree level is used) is robust but slow (55s, 68s, and 313s for these three models, respectively) and not sufficiently accurate (see the eye areas of the Camel and Cow). (b,c): our local cubic polynomial fitting is more accurate and much faster; (b): three-ring vertex neighborhood is used for polynomial fitting (2.24s, 2.98s, and 13.7s); (c): one-ring vertex neighborhood is used for polynomial fitting (0.66s, 0.85s, and 3.77s). (d): Crest line detection based on the curvature tensor fitting of (Rusinkiewicz, 2004) is even faster (0.15s, 0.17s, and 0.78s). (e): our focal surface based algorithm is sufficiently accurate and very fast (0.08s, 0.08s, and 0.35s).

and triangle soups. The main change required is to use an appropriate graph Laplacian instead of a mesh Laplacian. Graph Laplacians are now widely used in geometric data analysis and machine learning (Coifman et al., 2005) and their asymptotic properties are well understood (Coifman and Lafon, 2006; Singer, 2006) (see also references therein).

In this study, we have not utilized the full power of (6). Once $\mathbf{t}_{\max}$, $\mathbf{t}_{\min}$ and $e_{\max}$, $e_{\min}$ are found, (6) allows us to compute the remaining first-order curvature derivatives $\partial k_{\max}/\partial \mathbf{t}_{\min}$ and $\partial k_{\min}/\partial \mathbf{t}_{\max}$.

One limitation of our focal surface approach, the fastest crest line detection technique, consists of certain difficulties in estimating the curvature extremalities $e_{\max}$ and $e_{\min}$ in the mesh vertices close to the parabolic lines of surface $\mathbf{r}$. Indeed, each

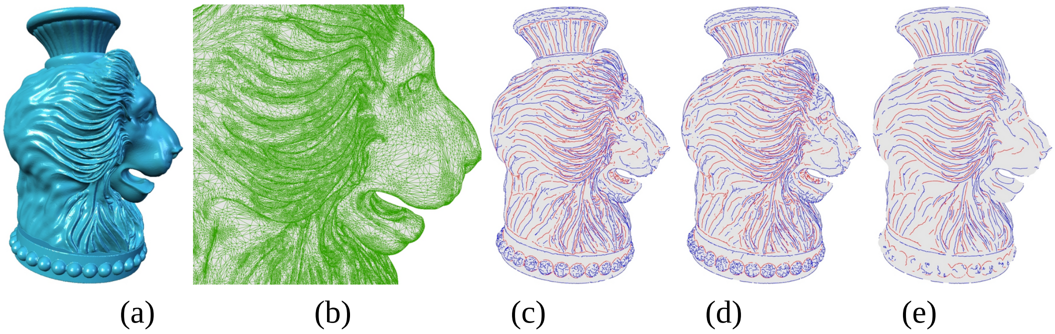

Figure 17. Detecting the crest lines on an irregular mesh model. No smoothing is applied to the mesh $\mathcal{M}$ for (c). Simple parameter-free smoothing of the mesh $\mathcal{M}$ is used to generate (d). Finally (e) is obtained from (d) by filtering the detected crest lines by T_1 defined in (24). Here the focal surface based finite difference scheme is employed to estimate curvature tensor and extremalities.

focal surface goes to infinity at the points of its corresponding parabolic line on $\mathbf{r}$. In practice, it affects very slightly our method for detecting the crest lines since they do not cross the parabolic lines. Nevertheless, if an estimation of $e_{\max}$ and $e_{\min}$ is required at a parabolic point, we can apply an inversion and then use (16) for estimating the corresponding curvature derivatives.

In this paper, we have focused on crest line extraction and presented only one geometric modeling application the these fascinating surface features: adaptive mesh decimation. We hope that our crest line detection approaches will be very useful for a number of shape interrogation and visualization tasks.

Our main mathematical contribution consists of discovering a series of Möbius-invariant surface-based differential forms and we expect that it will assist to further penetration and use of ideas and methods of Möbius differential geometry in geometric modeling and computer graphics areas.

To conclude, this work contributes to a computer-aided renaissance of the local differential geometry of curves and surfaces, a field with a surprising richness of ideas and results.

Acknowledgements

We are grateful to Szymon Rusinkiewicz and Yutaka Ohtake for making their source codes available. We would like to thank the anonymous reviewers of this paper for their helpful comments and suggestions.

This work was supported in part by AIM@SHAPE, a Network of Excellence project (506766) within EU's Sixth Framework Programme, and Strategic Programs for R&D (President's Discretionary Fund) of RIKEN.

The models are courtesy of INRIA Sophia-Antpolis (Vase-Lion and Tile), MIT Computer Graphics Group (Horse), Caltech Multi-Res Modeling Group (Feline), MPI Informatik (Max-Planck Bust), Stanford University (Stanford Bunny), University of Washington (Mannequin Head), Cyberware (Igea), Kitware Inc. (Cow), Alexander Pasko (Robot Cat), Yutaka Ohtake (Moai), and AIM@SHAPE shape repository (Camel, Gearbox, and Rolling Stage).

References

Belyaev, A. G., Anoshkina, E. V., Kunii, T. L., 1997. Ridges, ravines, and singularities. In: *A. T. Fomenko, and T. L. Kunii*, Topological Modeling for Visualization. Springer, pp. 375–383, ch. 18.

Belyaev, A. G., Pasko, A. A., Kunii, T. L., 1998. Ridges and ravines on implicit surfaces. In: Proc. Computer Graphics International 1998. pp. 530–535.

Bloomenthal, J., 1994. An implicit surface polygonizer. In: Graphics Gems IV. Academic Press Professional, Inc., San Diego, CA, USA, pp. 324–349.

Bobenko, A. I., Schröder, P., 2005. Discrete willmore flow. In: Third Eurographics Symposium on Geometry Processing (SGP 2005). pp. 101–110.

Cazals, F., Faugère, J.-C., Pouget, M., Rouillier, F., October 2006a. The implicit structure of ridges of a smooth parametric surface. Computer Aided Geometric Design 23 (7), 582–598.

Cazals, F., Faugère, J.-C., Pouget, M., Rouillier, F., 2006b. Ridges and umbilics of polynomial parametric surfaces. In: Juettler, B., Piene, R. (Eds.), Computational Methods for Algebraic Spline Surfaces II. Springer, pp. 141–159.

Cazals, F., Pouget, M., September 2004a. Ridges and umbilics of a sampled smooth surface: a complete picture gearing toward topological coherence. Rapport de Recherche RR-5294, INRIA.

Cazals, F., Pouget, M., March 2004b. Smooth surfaces, umbilics, lines of curvatures, foliations, ridges and the medial axis: a concise overview. Rapport de Recherche RR-5138, INRIA.

Cazals, F., Pouget, M., 2005. Differential topology and geometry of smooth embedded surfaces: selected topics. Int. J. of Computational Geometry and Applications 15 (5), 511–536.

Chandru, V., Dutta, D., Hoffmann, C. M., October 1989. On the geometry of Dupin cyclides. The Visual Computer 5 (5), 277–290.

Coifman, R. R., Lafon, S., July 2006. Diffusion maps. Applied and Computational Harmonic Analysis 21 (1), 5–30.

Coifman, R. R., Lafon, S., Lee, A. B., Maggioni, M., Nadler, B., Warner, F., Zucker, S. W., 2005. Geometric diffusions as a tool for harmonic analysis and structure definition of data: Diffusion maps. PNAS 102 (21), 7426–7431.

DeCarlo, D., Finkelstein, A., Rusinkiewicz, S., Santella, A., 2003. Suggestive contours for conveying shape. ACM Transactions on Graphics 22 (3), 848–855, proc. ACM SIGGRAPH 2003.

Eisenhart, L. P., 1909. A treatise on the differential geometry of curves and surfaces. Ginn and Company.

Ferapontov, E. V., 2000. Lie sphere geometry and integrable systems. Tohoku Mathematical Journal 52, 199–233.

Foufou, S., Garnier, L., 2004. Dupin cyclide blends between quadric surfaces for shape modeling. Computer Graphics Forum 23 (3), 321–330, eurographics 2004 issue.

Garland, M., Heckbert, P., 1997. Surface simplification using quadric error metrics. In: Proceedings of ACM SIGGRAPH. pp. 209–216.

Goldfeather, J., Interrante, V., 2004. A novel cubic-order algorithm for approximating principal direction vectors. ACM Transactions on Graphics 23 (1), 45–63.

Guéziec, A., 1993. Large deformable splines, crest lines and matching. In: Proc. IEEE Fourth Int'l Conf. Computer Vision. pp. 650–657.

Hallinan, P. L., Gordon, G. G., Yuille, A. L., Giblin, P., Mumford, D., 1999. Two- and Tree-Dimensional Patterns of the Face. A K Peters.

Hertrich-Jeromin, U., 2003. Introduction to Möbius Diffrential Geometry. Cambridge University Press.

Hildebrandt, K., Polthier, K., Wardetzky, M., 2005. Smooth feature lines on surface meshes. In: Third Eurographics Symposium on Geometry Processing (SGP 2005). pp. 85–90.

Hoffman, D. D., Richards, W. A., 1985. Parts of recognition. Cognition 18, 65–96.

Hosaka, M., 1992. Modeling of Curves and Surfaces in CAD/CAM. Springer, Berlin.

Interrante, V., Fuchs, H., Pizer, S., 1995. Enhancing transparent skin surfaces with ridge and valley lines. In: Proc. IEEE Visualization 1995. pp. 52–59.

Joshi, P., Séquin, C., 2007. Energy minimizers for curvature-based surface functionals. Computer-Aided Design and Applications 4 (5), 607–618.

Kent, J. T., Mardia, K. V., West, J., 1996. Ridge curves and shape analysis. In: The British Machine Vision Conference 1996. pp. 43–52.

Kho, Y., Garland, M., 2003. User-guided simplification. In: ACM Symposium on Interactive 3D Graphics. Washington, D.C., USA, pp. 123–126.

Kim, S.-K., Kim, C.-H., 2006. Finding ridges and valleys in a discrete surface using a modified MLS approximation. Computer-Aided Design 38 (2), 173–180.

Koenderink, J. J., 1990. Solid Shape. MIT Press.

Lévy, B., Petitjean, S., Ray, N., Maillot, J., July 2002. Least squares conformal maps for automatic texture atlas generation. ACM Transactions on Graphics 21 (3), 362–371, proc. ACM SIGGRAPH 2002.

Little, J. J., Shi, P., 2001. Structural lines, TINs and DEMs. Algorithmica 30 (2), 243–263.

Lukács, G., Andor, L., 1998. Computing natural division lines on free-form surfaces based on measured data. In: Dæhlen, M., Lyche, T., Schumaker, L. L. (Eds.), Mathematical Methods for Curves and Surfaces II. Vanderbilt Univ. Press, pp. 319–326.

Max, N., 1999. Weights for computing vertex normals from facet normals. Journal of Graphics Tools 4 (2), 1–6.

Meyer, M., Desbrun, M., Schröder, P., Barr, A. H., 2003. Discrete differential-geometry operators for triangulated 2-manifolds. In: Hege, H.-C., Polthier, K. (Eds.), Visualization and Mathematics III. Springer, Berlin, pp. 35–57.

Monga, O., Benayoun, S., Faugeras, O., 1992. From partial derivatives of 3-D density images to ridge lines. In: Proc. CVPR'92. IEEE, pp. 354–359.

Moreton, H. P., Séquin, C. H., August 1992. Functional optimization for fair surface design. In: Proceedings of ACM SIGGRAPH. pp. 167–176.

Ohtake, Y., Belyaev, A., Seidel, H.-P., August 2004. Ridge-valley lines on meshes via implicit surface fitting. ACM Transactions on Graphics 23 (3), 609–612, proc. ACM SIGGRAPH 2004.

Pennec, X., Ayache, N., Thirion, J. P., 2000. Landmark-based registration using features identified through differential geometry. In: Bankman, I. N. (Ed.), Handbook of Medical Imaging. Academic Press, pp. 499–513.

Pinkall, U., Polthier, K., 1993. Computing discrete minimal surfaces and their conjugates. Experimental Mathematics 2 (1), 15–36.

Porteous, I. R., 1987. Ridges and umbilics of surfaces. In: Martin, R. R. (Ed.), The Mathematics of Surfaces II. Clarendon Press, Oxford, pp. 447–458.

Porteous, I. R., 1994. Geometric Differentiation for the Intelligence of Curves and Surfaces. Cambridge University Press, Cambridge.

Rusinkiewicz, S., 2004. Estimating curvatures and their derivatives on triangle meshes. In: Second International Symposium on 3D Data Processing, Visualization, and Transmission, (3DPVT'04). pp. 486–493.

Singer, A., July 2006. From graph to manifold Laplacian: The convergence rate. Applied and Computational Harmonic Analysis 21 (1), 128–134.

Stylianou, G., Farin, G., September/October 2004. Crest lines for surface segmentation and flattening. IEEE Transactions on Visualization and Computer Graphics 10 (5), 536–544.

Taubin, G., 2002. Dual mesh resampling. Graphical Models 64 (2), 94–113.

Thirion, J., 1996. The extremal mesh and the understanding of 3D surfaces. International Journal of Computer Vision 19 (2), 115–128.

Thirion, J.-P., Monga, O., Benayoun, S., Guéziec, A., Ayache, N., 1992. Automatic registration of 3D images using surface curvature. In: Mathematical Methods in Medical Imaging, SPIE vol. 1768. SPIE, pp. 206–216.

Wang, C. P., 1992. Surfaces in Möbius geometry. Nagoya Mathematical Journal 125, 53–72.

Watanabe, K., Belyaev, A. G., 2001. Detection of salient curvature features on polygonal surfaces. Computer Graphics Forum 20 (3), 385–392, eurographics 2001 issue.

Weatherburn, C. E., 1927. Differential Geometry of Three Dimensions, volume I. Cambridge University Press.

Weatherburn, C. E., 1930. Differential Geometry of Three Dimensions, volume II. Cambridge University Press.

Willmore, T. J., 2000. Surfaces in conformal geometry. Annals of Global Analysis and Geometry 18 (3-4), 255–264.

Yoshizawa, S., Belyaev, A., Seidel, H.-P., 2005. Fast and robust detection of crest lines on meshes. In: ACM Symposium on Solid and Physical Modeling (SPM 2005). pp. 227 – 232, technical sketch.

Yoshizawa, S., Belyaev, A., Yokota, H., Seidel, H.-P., 2007. Fast and faithful geometric algorithm for detecting crest lines on meshes. In: Pacific Graphics. pp. 231–237.

Yu, J., Yin, X., Gu, X., McMillan, L., Gortler, S., July 2007. Focal surfaces of discrete geometry. In: Fifth Eurographics Symposium on Geometry Processing (SGP 2007). Barcelona, Spain, pp. 23–32.